DR2011264

APPENDIX

Figure A1:

Surface dynamic topography (left) since the Eocene shows progressively increasing subsidence in the northeast of Australia as the continent drifts towards the subduction zones. Reconstructed continents and plate boundaries show the position of fossil subduction zones since the Eocene. Temperature cross-sections (right) since the Eocene shows slabs accumulating beneath the northeastern margin of Australia and beneath the Tasman Sea. Temperature cross-sections are plotted with non-dimensional depths and are overlain by the 660 and 410 phase changes, which are deflected by temperature anomalies. This model topography shows the case with 75°C (5%) hotter than average mantle (1500 °C) beneath the Antarctic continent.

Figure A2:

The location of data used in the paleo-shoreline analysis study [*DiCaprio et al.*, 2009a]. Circles indicate boreholes. Erosional areas are indicated by squares. Six basins are selected (white). Inset plots show a profile (black line) with the shelf break at 200 m depth (grey line). Vertical tick marks are at 1000 m intervals in each profile. The extent of the 200 m isobath is shaded grey.

1. NUMERICAL MODELS

1.1 Governing equations

We use the finite element package *CitcomS Version 2.2* [*Tan et al.*, 2006; *Zhong et al.*, 2000] from the Computational Infrastructure for Geodynamics (CIG) (http://geodynamics.org). We treat the mantle as an incompressible viscous fluid with thermal mantle convection described by the conservation of mass, momentum and energy. These equations are solved in a spherical shell while making the Boussinesq

approximation. The following equations are in the non-dimensional form where the summation over spatial indices i and j and time, t is implicit:

$$u_{i,i} = 0 \qquad (1)$$

$$-P_{,i} + (\eta u_{i,j} + \eta u_{j,i})_{,j} + \delta\rho g \delta_{ir} = 0 \qquad (2)$$

$$T_{,t} + u_i T_{,i} = \kappa T_{,ii} + H \qquad (3)$$

Where u_i is the velocity, P is the dynamic pressure, $\delta\rho$ is the density anomaly, g is the gravitational acceleration, η is the viscosity, T is the temperature, κ is the thermal diffusivity, and H is the heat production (assumed to vanish over the limited duration of our models).

The models include buoyancy forces associated with phase transitions between the upper and lower mantle, compositional variations and temperature. These density anomalies are given by:

$$\delta\rho = -\alpha\rho_0(T - T_1) + \delta\rho_{ph}\Gamma + \delta\rho_{ch}C \qquad (4)$$

where $\delta\rho_{ph}$ is the density jump across the phase change, Γ is the phase function, $\delta\rho_{ch}$ is the density difference between two compositions, C is the composition, α is the thermal expansivity, ρ_0 is the reference density, and T_1 is the surface temperature.

The mantle reference Rayleigh number is:

$$R_a = \frac{\rho_0 g \alpha \Delta T R_0^3}{\kappa \eta_0} \qquad (5)$$

where κ is the thermal diffusivity, ΔT is the superadiabatic temperature drop, η_0 is the reference dynamic viscosity, and R_0 is the radius of the earth. Parameters that are held constant are summarized in Table 1 while the non-dimensionalisation is described in Appendix 3.2.

Dynamic topography h, results from the vertical component of stress (σ_{rr}):

$$h = \frac{\sigma_{rr}}{\Delta\rho g} \qquad (6)$$

where $\Delta\rho$ is the density difference between mantle and the density of the overlying medium.

1.2 Model geometry and resolution

The models use coupled *CitcomS* solvers [*Tan et al.*, 2006] that allows the velocity and pressure field of a global low-resolution model to be used as the boundary conditions on the embedded solver. This provides more natural side and bottom boundary conditions on the regional solver than could be obtained with reflecting or periodic boundary conditions. Our global solver has the surface velocity imposed while the bottom boundary condition is no slip. Our regional model covers most of the present day Indo-Australian plate and part of the Pacific plate.

The globe is divided into 12 caps, containing 33 nodes in the two map and radial directions. The global model has a surface resolution of about 274 km extending from the surface to the core mantle boundary with a radial resolution of 87 km. The regional model consists of one cap with 247 nodes in the latitude and longitude directions and 65 nodes in the radial direction; the resolution at the surface is 64 km in longitude by 40 km in latitude, while extending from 64 km to 2250 km depth with a radial resolution of 33 km.

CitcomS uses regional meshes that are bounded by lines of constant latitude and longitude. During the Cretaceous, Australia was located close to the south pole so that if we choose a domain during the Cretaceous, the mesh would have been condensed at the pole. To avoid pole-refined meshing, we work in a reference frame that is rotated to the equator. This reference frame is defined by an initial rotation that is introduced at the root of the rotation tree hierarchy. We define the center of the region of interest as $135\,°E$, $37.5\,°S$ rotated to the equator. All relative plate motions remain invariant because all plates move relative to the root of the rotation tree hierarchy.

1.3 Mantle rheology

The viscosity of the mantle is strongly dependent on pressure, stress (strain rate), temperature, water, melt, grain size and composition [*Ranalli*, 1995]. However, including all these parameters in large-scale models is not currently feasible. Our models have a Newtonian viscosity that has temperature, depth, composition and position dependencies. The mantle is divided into four layers: lithosphere (0-100 km), upper mantle (100-410 km), transition zone (410-670 km), lower mantle (670-2880 km) and the viscosity of each layer is varied between models.

The temperature dependence of viscosity is:

$$\eta = \eta_0 e^{\left(\frac{A_e}{T+A_T} - \frac{A_e}{1+A_T}\right)} \qquad (7)$$

where η_0 is the reference viscosity, A_e is an effective non-dimensional activation energy, A_T is the temperature offset of 0.1 in each layer. The viscosity variation across the domain is between $2\times10^{19}\,Pas$ and $2\times10^{23}\,Pas$, consistent with observations of seismic strain rates [*Billen et al.*, 2003].

1.4 Variable phase change parameters

The transition zone is bounded in depth by two phase transitions that have both a Clapeyron slope and a density change. Recent studies suggest the Clapeyron slope at the 410 km phase change is between 2 and 4.0 MPa/K [*Katsura and Ito*, 1989; *Katsura et al.*, 2004; *Morishima et al.*, 1994]. The density difference associated with the 410 km phase change is approximately 100 kg/m^3 [*Bina and Helffrich*, 1994]. The Clapeyron slope at the 660 km phase change is between -0.5 and -4 MPa/K [*Fei et al.*, 2004; *Irifune et al.*, 1998; *Ito and Takahashi*, 1989; *Katsura et al.*, 2003; *Litasov et al.*, 2005]. The density difference at the 660 km phase change is about 236 kg/m^3 [*Ita and Stixrude*, 1992].

The Clapeyron slope of the phase changes bounding the transition zone influences the magnitude of surface topography. A steeper Clapeyron slope at the 410 km phase change

(olivine to spinel) results in a greater downward body force driving flow within the cold slab and produces a larger effect on surface topography. By contrast, a steeper Clapeyron slope at the 660 km phase change (spinel to perovskite-magnesiowüstite) inhibits flow and results in less dynamic surface topography. We alter the phase change parameters while ensuring they are consistent with seismological observations and high-pressure experiments. The values used in each model are listed in Table 2.

1.5 Tracers

We use passive tracers to map the motion of Pacific and Indian mantle domains for models that start at 140 Ma. We use active tracers within the continental lithosphere to provide buoyancy and within the mantle wedge to lower the viscosity. The area of the Indian and Pacific mantle domains is delimited by the initial slab location and dip extending to the CMB on the eastern margin of Australia. To the east of the slab is the Pacific mantle domain and to the west is the Indian mantle domain. The extent of all tracers is limited by the regional box boundaries with 18 tracers per element.

Continental stability is maintained through compositionally buoyancy that tends to counteract the negative buoyancy of the continental lithosphere [*Jordan*, 1979] and use buoyant tracers to simulate this process. The average density beneath the continental cratonic crust is 3300 kg/m3 [*Dziewonski and Anderson*, 1981] [*Kaban et al.*, 2003] and we use an average density of 3500 kg/m3 within the asthenosphere. We define the buoyancy of continental lithosphere using the ratio method [*McNamara and Zhong*, 2004]:

$$B = \frac{Ra_c}{Ra} \text{ where } Ra_c = Ra\frac{\delta\rho_c}{\rho_0} \qquad (8)$$

The distribution of continental tracers is defined by continental crust and arc fragments from oceanic paleo age grids [*Müller et al.*, 2008b] over a depth of 180 km based on an average seismic depth of cratonic and Phanerozoic lithospheric elements in Australia [*Kennett*, 2003].

During subduction water is released into the upper 200 km of the mantle wedge from the downgoing slab, primarily from hydrated basalts [*Peacock*, 1990; *Ranero et al.*, 2003] and a thin veneer of pelagic sediments. Due to the presumed high concentrations of water and melt in the mantle wedge, the viscosity of the mantle wedge may be reduced by at least an order of magnitude compared to the surrounding asthenosphere [*Baker-Hebert et al.*, 2009; *Billen and Gurnis*, 2001]. This low viscosity can significantly reduce the magnitude of negative dynamic topography and the geoid by decreasing the coupling between the slab and the overriding plate [*Billen et al.*, 2003].

We use tracers to reduce the viscosity within the mantle wedge by a factor of 10 compared to the surrounding asthenosphere. The spatial distribution of mantle wedge tracers is defined by the initial slab location and dip. The depth extent of low seismic velocities assumed to be associated with the low viscosity wedge are typically 150 km above the slab but may extend to 400 km depth below the backarc [*Wiens and Smith*, 2003]. Our wedge extends from the surface to 400 km with a lateral extent of 350 km for a slab with a 50° dip.

2. ASSIMILATED DATA

2.1 Plate Kinematics

Plate motion is imposed as a velocity boundary condition using a model of continuously evolving plate boundaries whose motions are determined in a moving hotspot reference frame. We use *GPlates* software [*Boyden et al.*, 2009; *Gurnis et al.*, 2009] to reconstruct rigid plates with continuously evolving plate boundaries back to 140 Ma. Plate boundaries were used to create closed plate polygons [*Gurnis et al.*, 2009], which define the instantaneous plate velocity at 1 Myr time increments on both the global and regional *CitcomS* meshes.

Plate boundaries consist of mid-ocean ridges, subduction zones and transform faults. The position of mid-ocean ridges is found using the half-stage rotation reconstructed from magnetic lineations and the relative rotation between the two diverging plates. Fracture and subduction zones were positioned according to common reconstructions and

reported preserved arc materials (Appendix 3). The rotation of these subduction zones is based on the overriding plate where no other rotation has been determined. Our reconstructions use a moving hotspot absolute plate motion reference frame [*O'Neill et al.*, 2003] from 100 Ma to the present; they use a fixed hotspot reference frame from 140 to 100 Ma [*Müller et al.*, 2008a]. The global plate motions are described by relative plate motion models summarized by Müller et al., [2008a].

2.2 Seafloor age

The reconstructed ages of the ocean floor [*Müller et al.*, 2008b], consistent with the continuously closed plate model, is assimilated into the models as a surface temperature boundary condition every 1 Myr. We use a half-space model to calculate the temperature based on the age of the oceanic crust:

$$T^{HS} = T_s + (T_m - T_s) erf\left(\frac{y}{2\sqrt{\kappa t}}\right) \qquad (9)$$

where T_s is the surface temperature (here set to non-dimensional value of 0), T_m is the ambient mantle temperature, t is time, and y is the depth. Temperature is assimilated as a linear function of depth, y , with a cutoff depth (y_p) of 80 km:

$$T_{i+1} = aT_i + (1-a)T_{i+1}^{HS} \text{ where } a = \begin{cases} \dfrac{y}{y_p} & y < y_p \\ 1 & y \geq y_p \end{cases} \qquad (10)$$

where T_i is the model temperature at timestep i and T_{i+1}^{HS} is the temperature found from the half space cooling model.

2.3 Backarc basins

Subduction-induced flow caused by the downgoing plate produces a net upward suction force on the slab that is thought to be balanced by the gravitational body force of the slab [*Stevenson and Turner*, 1977; *Tovish et al.*, 1978]. However, in purely viscous models, the broadening of the slab produces an overwhelming suction force causing the slab to be pulled up towards the overriding plate [*Christensen*, 1996; *Manea and Gurnis*, 2007]. The coupling of the slab to the overriding plate is resolved when a more realistic mantle wedge rheology is included into dynamic models [*Billen and Hirth*, 2007; *Manea and*

Gurnis, 2007] which is suitable for higher resolution, detailed models of subduction zone dynamics. However, in larger scale models, the slab suction problem can be resolved by removing the overriding plate and applying a velocity in the backarc that is trench perpendicular towards the converging margin [*Christensen*, 1996; *Tan et al.*, 2002]. Here we set the backarc region to ambient mantle temperature and impose a backarc velocity in order to insert a realistic slab into the upper mantle. The amplitude of this imposed velocity within the backarc is approximately equal but opposite to the velocity of the downgoing plate at the trench.

2.4 Initial slab parameters

We thermally prescribe a subducting slab as an initial condition. The slab has either a deep dip of 30° or 50° and is vertical in the lower mantle. The temperature profile of the slab is symmetric about its center, set to 0. The temperature gradient from its center is calculated using the half-space cooling model (equation 8), the age of the sea floor sampled at the trench, and the distance from the center of the slab.

We impose the slabs at 50 Ma at the reconstructed subduction zones surrounding the Australian continent in order to investigate the large scale, progressive tilt of the continent since the Eocene.

During the early Eocene NE-dipping subduction was located north of New Caledonia [*Aitchison et al.*, 1995; *Cluzel et al.*, 2001; *Crawford et al.*, 2003; *Spandler et al.*, 2005] producing the Eocene volcanic arc (Loyalty Ridge). This subduction may have been active since the Late Cretaceous [*Crawford et al.*, 2003; *Eissen et al.*, 1998; *Schellart et al.*, 2006] and may have continued southward into the Norfolk Basin along the Three Kings Ridge [*DiCaprio et al.*, 2009b; *Meffre et al.*, 2006; *Mortimer et al.*, 2007]. We place an initial slab to the east of New Caledonia and extending into the Norfolk Basin. The slab extends into the upper mantle to 400 km depth.

Between 50 and 45 Ma southwest-dipping subduction at the Melanesian arc was initiated [*Gaina and Müller*, 2007; *Hall*, 2002]. This subduction was preceded by N-

dipping subduction north of Australia. We place an initial slab at the Melanesian arc and assume that the initial slab extends to 300 km depth.

3. MODELING PARAMETERS

Table 1: Parameters held constant within the models

Parameter	**Notation**	**value**
Reference mantle density	ρ_0	$3500\,kg/m^3$
Gravity	g	$10\,m/s^2$
Temperature of the surface	T_0	$0\,°C$
Change in temperature from the CMB to the surface	ΔT	$1500\,°C$
Radius	R_0	$6371000\,m$
Coefficient of thermal expansion	α	$2\times10^{-5}\ K^{-1}$
Thermal diffusivity	κ	$1\times10^{-6}\ m^2/s$
Reference viscosity	η_0	$2\times10^{21}\ Pas$
Rayleigh number	$R_a=\frac{\rho_0 g\alpha_0 \Delta T R_0^3}{\kappa_0\eta_0}$	$R_a=1.3576\times10^{+08}$

Table 2: Geodynamic models and properties

Model Name	Non-dimensional Viscosity layers	Dip	Start age	Slope 410 (MPa/K)	Slope 660 (MPa/K)
M1	100,1,5,10	50	50	4	-2
M2	100,1,5,10	50	50	4	-4
M3	100,1,5,10	50	50	2	-4
M4	100,1,5,10	50	50	2.9	3

3.2 Dimensional and non-dimensional parameters used in models

3.2.1 Reference Rayleigh Number

R_a is the whole mantle Rayleigh number which is defined as:

$$R_a = \frac{\rho_0 g \alpha_0 \Delta T R_0^3}{\kappa_0 \eta_0}, \quad R_a = 1.3576 \times 10^{+08}$$

3.2.2 Phase change

The buoyancy of the transition zone is defined by the Clapeyron slope and the density change. The density change is expressed within the phase change Rayleigh number.

Phase change Rayleigh number

The density change at the 410 km transition (olivine – wadsleyite) is between 3% and 5%. The density change at the 660 km transition (ringwoodite-perovskite) is between 7% - 9.3 % (Dziewonski and Anderson, 1981;Kennett, et al., 1995;Weidner and Wang., 1998). The Rayleigh number of the phase change is defined as: $R_{ph} = R_a \left(\frac{\Delta \rho_{ph}}{\rho_0} \right) = \frac{\Delta \rho_{ph} g R^3}{\eta \kappa}$

Table 3: Rayleigh numbers used at the 660 km and 410 km transition zones

Mineral change	% $\Delta\rho$	$\Delta\rho\left(kgm^{-3}\right)$	R_{ph}	Reference

410 km Olivine-Wadsleyite	3.0-5.7	100	R_{ph410} 1.293e+08	(Bina and Helffrich, 1994)
660 km Ringwoodite-Perovskite	7.0-9.3	236	R_{ph660} 3.05e+08	(Akaogi and Ito, 1999)

3.2.3 Clapeyron slope

The clapeyron slope at the 410 km transition (olivine-wadsleyite) is 2.5 – 4.0 MPa/K (Katsura and Ito, 1989;Katsura, et al., 2004;Morishima, et al., 1994). The clapeyron slope at the 660 km transition (ringwoodite-perovskite) is between -0.5 and -3.0 MPa/K (Fei, et al., 2004;Irifune, et al., 1998;Ito and Takahashi, 1989;Katsura, et al., 2003;Litasov, et al., 2005). The clapeyron slope is defined as $\frac{d\mathrm{P}}{d\mathrm{T}}$ and is non-dimensionalised using $\gamma = \frac{\rho_0 g_0 R_0}{\Delta \mathrm{T}} \gamma'_{ph}$ where γ' is the non-dimensionalised slope.

Table 4: This is an example of the ranges and values used for the 410 km and 660 km Clapeyron slopes

Mineral change	γ **(MPa/K)**	γ **used**	γ'	**Reference**
410 km Olivine-Wadsleyite	2.5 to 4.0	4.0	0.0269	(Katsura and Ito, 1989;Katsura, et al., 2004;Morishima, et al., 1994)
660 km Ringwoodite-Perovskite	-0.5 to -3.0	-2.0	-0.0135	(Fei, et al., 2004;Irifune, et al., 1998;Ito and Takahashi, 1989;Katsura, et al., 2003;Litasov, et al., 2005)

3.2.4 Temperature change of phase change

The temperature change at the phase change is described by $\mathrm{T}_0 = \Delta \mathrm{T} \mathrm{T}'_0$ where $\mathrm{T}'_0 = 0.1821$. The temperature is non-dimensionalised by $\mathrm{T} = \Delta \mathrm{T}(\mathrm{T}' + \mathrm{T}'_0)$.

Mineral change	$T(C°)$	**Reference**	T

410 km Olivine-Wadsleyite	1673-1923	(Bina and Helffrich, 1994)	0.9332
660 km Ringwoodite-Perovskite	1673-1923	(Bina and Helffrich, 1994)	0.9332

3.2.5 Viscosity

Viscosity in our models is both temperature and depth dependent. Viscosity is non-dimensionalised using $\eta' = \frac{\eta}{\eta_0}$ where η_0 is the reference viscosity $\eta_0 = 2e^{+21}$, and η is dimensionalised viscosity. The minimum viscosity is set to 0.01 (2×10^{19}) and we limit the maximum viscosity to be 2×10^{23} in order for modeled slab viscosity to be consistent with observations of dynamic topography and the geoid in active subduction zones (Billen, et al., 2003). We impose a layered viscosity mantle. It is thought that the upper mantle is weak in order to account for post glacial rebound and geoid anomalies (Hager and Richards, 1989) and (Mitrovica and Forte 1997) .

3.2.6 Temperature dependence of viscosity

The temperature dependence of viscosity is governed by the following viscosity law:

$Viscosity = \eta_0 e^{\left(\frac{A_e}{T+A_T} - \frac{A_e}{1+A_T}\right)}$ where η_0 is the reference viscosity, η_e is the activation energy, η_T is the temperature offset of each layer. This has the effect of producing structures with shorter wavelengths (Zhong, *et al.*, 2000). We use the following activation energy and temperature offset for each layer:

Table 5: Activation energy and temperature offset for each layer

$A_{e\,0-100}$	$A_{e\,100-410}$	$A_{e\,410-660}$	$A_{e\,660-CMB}$
11	11	11	11
$A_{t\,0-100}$	$A_{t\,100-410}$	$A_{t\,410-660}$	$A_{t\,660-CMB}$
0.1	0.1	0.1	0.1

3.2.7 Cratons and compositional buoyancy

The density change due to a chemical change of viscosity is given by $\delta\rho = \delta\rho_{ch} C$. The typical density of the lithospheric mantle beneath cratons is: $\rho_{ch} = 3300$. $\delta\rho_{ch}$ is the density contrast between different chemical components, C is the composition (some factor), $\delta\rho$ is the thermal change in density.

$$\delta\rho = \rho_0 \Delta T \alpha$$
$$\delta\rho = 3500 \times 1500 \times 2 \times 10^{-5}$$
$$\delta\rho = 105$$

$$\delta\rho_{ch} = 3500 - 3300 = 200$$
$$C = \frac{\delta\rho}{\delta\rho_{ch}} = \frac{105}{200} = 0.5250$$

3.2.8 The Chemical Rayleigh number and buoyancy ratio

The chemical Rayleigh number is given by:

$$Rac = Ra \frac{\delta\rho_{ch}}{\rho_0}$$
$$Rac = \frac{\Delta\rho g R^3}{\eta\kappa}$$
$$Rac = \frac{200 \times 10 \times 6371000^3}{1 \times 10^{-6} \times 2 \times 10^{21}}$$
$$Rac = 2.5860 \times 10^8$$

The buoyancy ratio (B), is a non-dimensional quantity which is the ratio of chemical to thermal buoyancy (McNamara and Zhong, 2004).

$$B = \frac{Rac}{Ra}$$
$$B = \frac{\Delta\rho_{ch}}{\Delta\rho}$$
$$B = \frac{2.586 \times 10^{+08}}{1.3576e^{+08}}$$
$$B = 1.9048$$

Aside:

$$\alpha = \frac{1}{V}\frac{\partial V}{\partial T}$$

$$V = \frac{m}{\rho}$$

$$\frac{\partial V}{\partial T} = m\frac{\partial}{\partial T}\left(\frac{1}{\rho}\right)$$

$$\frac{\partial V}{\partial T} = m(-1)\rho^{-2}\frac{\partial \rho}{\partial T}$$

$$\alpha = \frac{\rho}{m}m(-1)\rho^{-2}\frac{\partial \rho}{\partial T}$$

$$\alpha = \rho^{-1}\frac{\partial \rho}{\partial T}$$

$$\Delta\rho = \rho_0 \Delta T \alpha$$

References

Aitchison, J. C., et al. (1995), Eocene arc-continent collision in New Caledonia and implications for regional southwest Pacific tectonic evolution, *Geology*, *23*, 161-164.

Baker-Hebert, L., et al. (2009), Emergence of a low-viscosity channel in subduction zones through the coupling of mantle flow and thermodynamics, *Earth and Planetary Science Letters*, *278*(3-4), 243-256.

Billen, M., and G. Hirth (2007), Rheologic controls on slab dynamics, *Geochemistry Geophysics Geosystems*, *8*(Q08012).

Billen, M. I., and M. Gurnis (2001), A low viscosity wedge in subduction zones, *Earth and Planetary Science Letters*, *193*(1-2), 227-236.

Billen, M. I., et al. (2003), Multiscale dynamics of the Tonga–Kermadec subduction zone, *Geophysical Journal International*, *153*, 359-388.

Bina, C. R., and G. Helffrich (1994), Phase transition Clapeyron slopes and transition zone seismic discontinuity topography, *Journal of Geophysical Research*, *99*(B8), 15,853-815,860.

Boyden, J., et al. (2009), Next-generation plate-tectonic reconstructions using GPlates, in *Geoinformatics: Cyberinfrastructure for the Solid Earth Sciences*, edited by G. R. Keller and C. Baru, Cambridge University Press, in preparation, Cambridge.

Christensen, U. R. (1996), The influence of trench migration on slab penetration into the lower mantle, *Earth and Planetary Science Letters*, *140*(1-4), 27-39.

Cluzel, D., et al. (2001), Tectonic accretion and underplating of mafic terranes in the late Eocene intraoceanic fore-arc of New Caledonia (Southwest pacific):Geodynamic implications., *Tectonophysics*, *340*, 23–59.

Crawford, A. J., et al. (2003), 120 to 0 Ma tectonic evolution of the southwest Pacific and analogous geological evolution of the 600 to 220 Ma Tasman Fold Belt system., in *Evolution and dynamics of the Australian Plate*

, edited by R. R. Hills and R. D. Muller, pp. 377-397, Geological Society of Australia Special Publication 22 and Geological Society of America Special Paper 372.

DiCaprio, L., et al. (2009a), Long-wavelength tilting of the Australian continent since the Late Cretaceous, *Earth and Planetary Science Letters*, *278*, 175-185.

DiCaprio, L., et al. (2009b), Linking active margin dynamics to overriding plate deformation: Synthesizing geophysical images with geological data from the Norfolk Basin., *Geochemistry Geophysics Geosystems*, *10*.

Dziewonski, A. M., and D. L. Anderson (1981), Preliminary reference Earth model, *Physics of the Earth and Planetary Interiors*, *25*, 297–356.

Eissen, J.-P., et al. (1998), Geochemistry and tectonic significance of basalts in the Poya Terrance, New Caledonia, *Tectonophysics*, *284*, 203-219.

Fei, Y., et al. (2004), Experimentally determined postspinel transformation boundary in Mg2SiO4 using MgO as an internal pressure standard and its geophysical implications. , *Journal of Geophysical Research*, *109*.

Gaina, C., and R. D. Müller (2007), Cenozoic tectonic and depth/age evolution of the Indonesian gateway and associated back-arc basins, *Earth Science Reviews*, *in press*.

Gurnis, M., et al. (2009), Global Plate Reconstructions with Continuously Closing Plates, *Geochemistry, Geophysics, Geosystems submitted*, *Special theme "Plate Reconstructions, Mantle Convection, and Tomography Models: A Complementary Vision of Earth's Interior"*.

Hall, R. (2002), Cenozoic geological and plate tectonic evolution of SE Asia and the SW Pacific: computer-based reconstructions, model and animations, *Journal of Asian Earth Sciences*, *20*, 353-431.

Irifune, T., et al. (1998), Postspinel phase boundary in Mg2SiO4 determined by in situ X-ray measurement., *Science*, *279*, 1698–1700.

Ita, J. J., and L. Stixrude (1992), Petrology, elasticity, and composition of the mantle transition zone,, *Journal of Geophysical Research*, *97*, 6849-6866.

Ito, E., and E. Takahashi (1989), Post-spinel transformations in the system Mg2SiO4-Fe2SiO4 and some geophysical implications, *Journal of Geophysical Research*, *94*, 10637–10646.

Jordan, T. H. (1979), Mineralogies, densities and seismic velocities of garnet lherzolites and their geophysical implications. , in *The mantle sample: inclusions in kimberlites and*

other volcanics, edited by F. R. Boyd and H. O. A. Meyer, pp. 1-14, Proc. 2nd Intern. Kimberlite Conf. .

Kaban, M. K., et al. (2003), Density of the continental roots: compositional and thermal contributions, *Earth and Planetary Science Letters*, *209*(1-2), 53-69

Katsura, T., and E. Ito (1989), The system Mg2SiO4-Fe2SiO4 at high pressures and temperatures:precise determinations of stabilities of olivine, modified spinel, and spinel, *Journal of Geophysical Research*, *94*(15), 663–670.

Katsura, T., et al. (2003), Post-spinel transition in Mg2SiO4 determined by high p-t in-situ X-ray diffractometry., *Physics of the Earth and Planetary Interiors*, *136*, 11-24.

Katsura, T., et al. (2004), Olivinewadsleyite transition in the system (Mg,Fe)2SiO4., *Journal of Geophysical Research*, *109*(B02209).

Kennett, B. L. N. (2003), Seismic structure in the mantle beneath Australia, in *Evolution and Dynamics of the Australian Plate*, edited by R. R. Hillis and R. D. Muller, pp. 7-23, Geological Society of Australia Special Publication 22 and Geological Society of America Special Paper 372, Sydney.

Litasov, K., et al. (2005), In situ X-ray diffraction study of postspinel transformation in a peridotite mantle: implications for the 660-km discontinuity., *Earth and Planetary Science Letters*, *238*, 311-328.

Manea, V., and M. Gurnis (2007), Subduction zone evolution and low viscosity wedges and channels, *Earth and Planetary Science Letters*, *264*, 22–45.

McNamara, A. K., and S. Zhong (2004), Thermochemical structures within a spherical mantle: Superplumes or Piles?, *Journal of Geophysical Research*, *109*(B07402).

Meffre, S., et al. (2006), Arc-continent collision forming a large island between New Caledonia and New Zealand in the Oligocene., paper presented at Australian Earth Science Convention., Melbourne.

Morishima, H., et al. (1994), The phase boundary between α- and β-Mg2SiO4 determined by in situ X-ray observation., *Science*, *265*, 1202–1203.

Mortimer, N., et al. (2007), Oligocene-Miocene tectonic evolution of the South Fiji Basin and Northland Plateau, SW Pacific Ocean: evidence from petrology and dating of dredged rocks., *Marine Geology.*, *237*, 1–24.

Müller, R. D., et al. (2008a), Age, spreading rates and spreading asymmetry of the world's ocean crust, *Geochemistry, Geophysics, Geosystems*, *9*(Q04006).

Müller, R. D., et al. (2008b), Long-Term Sea-Level Fluctuations Driven by Ocean Basin Dynamics, *Science*, *319*(5868), 1357 - 1362.

O'Neill, C., et al. (2003), Geodynamic implications of moving Indian Ocean hotspots, *Earth And Planetary Science Letters*, *215*(1-2), 151-168.

Peacock, S. (1990), Fluid processes in subduction zones, *Science*, *248*, 329–337.

Ranalli, G. (1995), *Rheology of the earth*, 2 ed., Chapman & Hall, London.

Ranero, C., et al. (2003), Bending-related faulting and mantle serpentinization at the Middle America trench, *Nature*, *425*, 367–373.

Schellart, W. P., et al. (2006), A Late Cretaceous and Cenozoic reconstruction of the Southwest Pacific region: Tectonics controlled by subduction and slab rollback processes, *Earth-Science Reviews*, *76*(3-4), 191-233.

Spandler, C., et al. (2005), Late cretaceous-tertiary tectonics of the southwest pacific: Insights from u-pb sensitive, high-resolution ion microprobe (shrimp) dating of eclogite facies rocks from new caledonia, *Tectonics*, *24*.

Stevenson, D. J., and J. S. Turner (1977), Angle of subduction, *Nature*, *270*, 334-336.

Tan, E., et al. (2002), Slabs in the lower mantle and their modulation of plume formation, *Geochemistry Geophysics Geosystems*, *3*(11), 1067.

Tan, E., et al. (2006), GeoFramework: Coupling multiple models of mantle convection within a computational framework, *Geochemistry, Geophysics, Geosystems 7*.

Tovish, A., et al. (1978), Mantle flow pressure and the angle of subduction: non-Newtonian corner flows, *Journal of Geophysical Research*, *83*, 5892-5898.

Wiens, D. A., and G. P. Smith (2003), Seismological constraints on structure and flow patterns within the mantle wedge, in *Inside the subduction factory*, edited by J. Eiler, Geophysical Monograph, American Geophysical Union, Washington DC.

Zhong, S. J., et al. (2000), Role of temperature-dependent viscosity and surface plates in spherical shell models of mantle convection, *Journal of Geophysical Research- Solid Earth*, *105*(B5), 11063-11082.

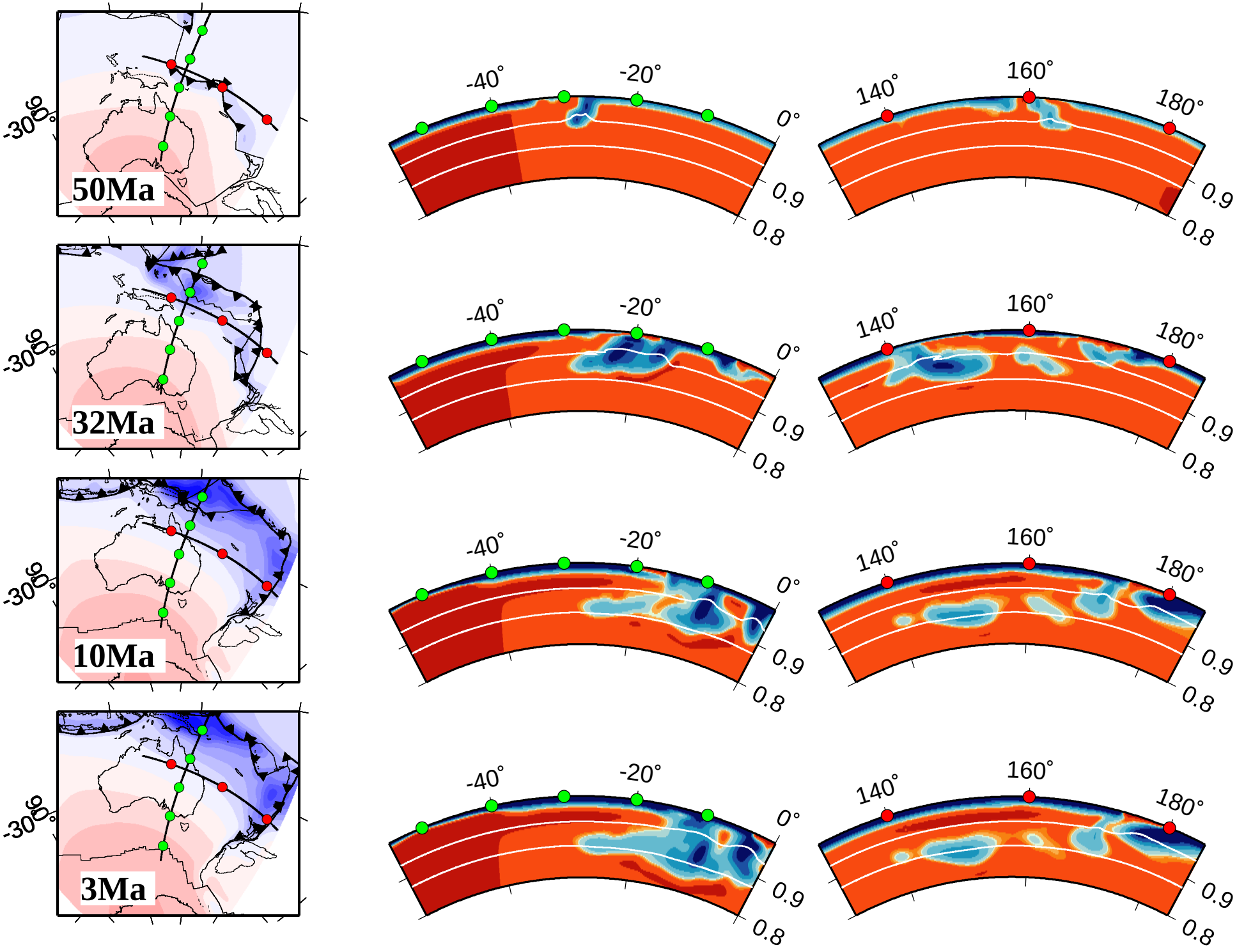
50Ma
32Ma
10Ma
3Ma
-30°
-40°
-20°
0°
140°
160°
180°
0.9
0.8
topography (m)
-1000
0
1000
temperature
0.0
0.5
1.0

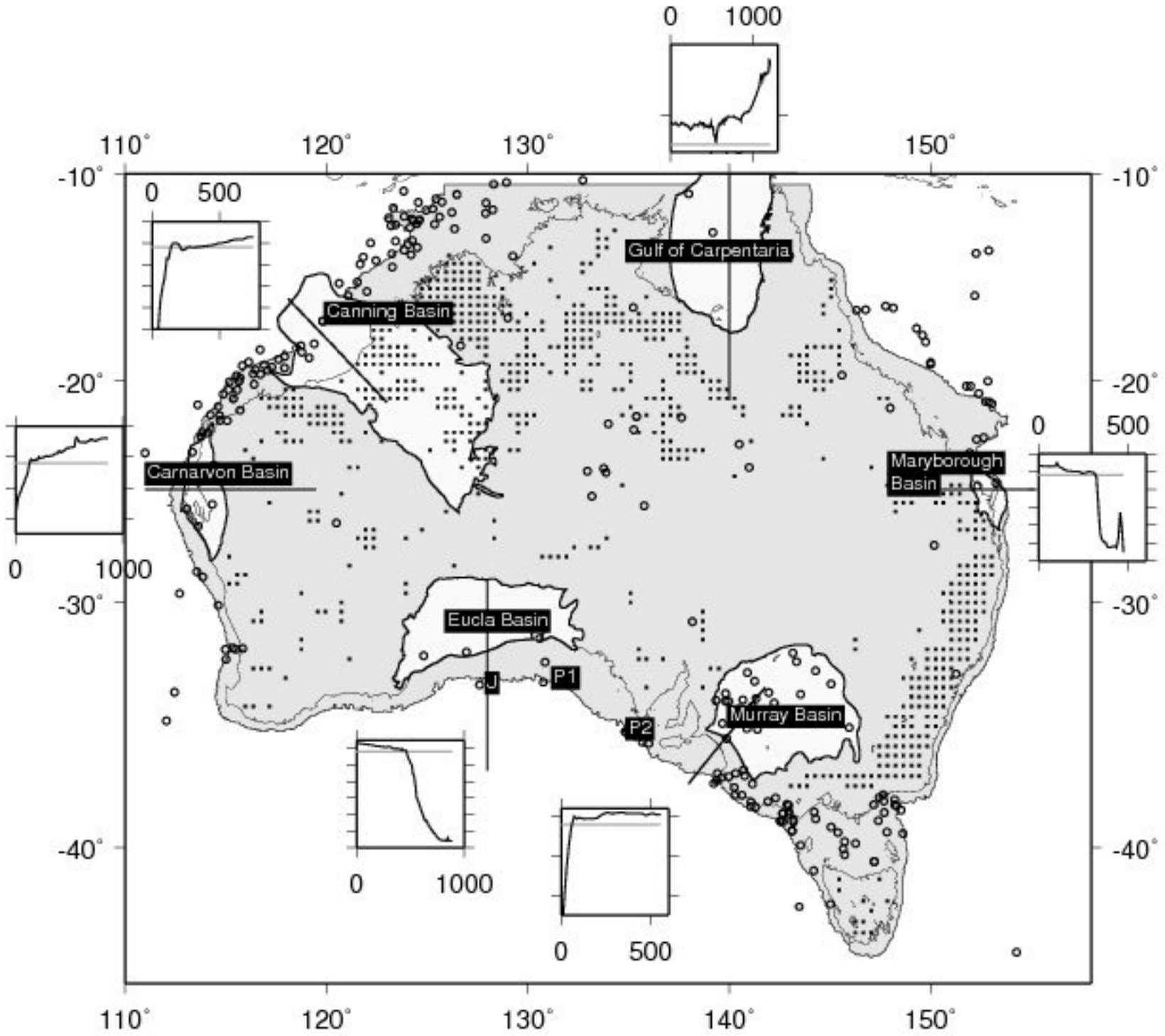
0
1000
110°
120°
130°
150°
-10°
0
500
Gulf of Carpentaria
Canning Basin
-20°
0
500
Carnarvon Basin
Maryborough
Basin
0
1000
-30°
Eucla Basin
J
P1
P2
Murray Basin
-40°
0
1000
0
500
110°
120°
130°
140°
150°